MEDICAL ROBOTS

Human adipose–derived mesenchymal stem cell–based medical microrobot system for knee cartilage regeneration in vivo

Copyright © 2020 The Authors, some rights reserved; exclusive licensee American Association for the Advancement of Science. No claim to original U.S. Government Works

Gwangjun Go[1,2]*, Sin-Gu Jeong[3]*, Ami Yoo[1], Jiwon Han[1], Byungjeon Kang[1], Seokjae Kim[1], Kim Tien Nguyen[1,2], Zhen Jin[4], Chang-Sei Kim[1,2], Yu Ri Seo[5], Ju Yeon Kang[5], Ju Yong Na[5], Eun Kyoo Song[5], Yongyeon Jeong[6], Jong Keun Seon[5†], Jong-Oh Park[1,2†], Eunpyo Choi[1,2†]

Targeted cell delivery by a magnetically actuated microrobot with a porous structure is a promising technique to enhance the low targeting efficiency of mesenchymal stem cell (MSC) in tissue regeneration. However, the relevant research performed to date is only in its proof-of-concept stage. To use the microrobot in a clinical stage, biocompatibility and biodegradation materials should be considered in the microrobot, and its efficacy needs to be verified using an in vivo model. In this study, we propose a human adipose–derived MSC–based medical microrobot system for knee cartilage regeneration and present an in vivo trial to verify the efficacy of the microrobot using the cartilage defect model. The microrobot system consists of a microrobot body capable of supporting MSCs, an electromagnetic actuation system for three-dimensional targeting of the microrobot, and a magnet for fixation of the microrobot to the damaged cartilage. Each component was designed and fabricated considering the accessibility of the patient and medical staff, as well as clinical safety. The efficacy of the microrobot system was then assessed in the cartilage defect model of rabbit knee with the aim to obtain clinical trial approval.

INTRODUCTION

In recent years, cell-based therapy for cartilage repair has made technological advances to fabricate commercial products and become a promising treatment with artificial joint transplant and marrow stimulation technique (*1*–*3*). In particular, there is considerable interest in the application of mesenchymal stem cells (MSCs) with multilineage differentiation potential among cells used in cartilage regeneration (*4*, *5*). MSCs can induce peripheral tolerance and migrate to injured tissues, preventing arthritis by relieving inflammation and treating joint cartilage through chondrogenic differentiation to avoid or delay joint replacement surgery (*2*). Knee cartilage regeneration with MSCs is accomplished through intra-articular injection or scaffold implantation into the defect (*6*–*8*). MSC-based medicine has already demonstrated notable cartilage regeneration in many case studies (*8*, *9*). However, because of low targeting efficiency of MSCs, the current MSC-based therapy requires a large amount of cells for intra-articular injection or invasive surgery for scaffold implantation above the millimeter size.

To improve the lack of targeting efficiency for the present MSC-based therapy, some research groups suggested a magnetically actuated microrobot for targeted MSC delivery (*10*–*14*). The microrobot not only supports the MSC through a porous structure but also precisely delivers MSCs to the defect site by untethered motion using an electromagnetic actuation (EMA) system consisting of multiple electromagnetic coils. Furthermore, the small microrobot size helps avoid invasive surgery through a needle-based injection (*15*). Although these microrobots have demonstrated their biocompatibility, cell-carrying capacity, and cell transport in vitro or in simple in vivo environments, the following two crucial requirements should be further considered to approach the clinical stage: (i) Clinically safe materials, such as U.S. Food and Drug Administration (FDA)–approved biocompatible and biodegradable materials, should be used. Current microrobots are composed of nondegradable materials or materials whose clinical safety has not been fully verified. If the microrobot is not released ex vivo or metabolized by the body, such materials may accumulate in the organ and cause chronic inflammatory responses (*16*). For example, a magnetic microrobot, which consists of SU-8 microstructure using three-dimensional (3D) laser lithography, Ni for magnetic actuation, and Ti for biocompatibility, was proposed for MSC transport (*10*, *11*). Although the microrobot serves magnetic drive and biocompatibility, its materials are not biodegradable and remain permanently in the body. (ii) The targeting and regeneration effects of microrobots using the in vivo model of appropriated disease should be fully verified considering the complete clinical environment, such as medical staff, patients, and imaging devices. Recent studies of the MSC-based therapy using the EMA system demonstrated the feasibility of cartilage regeneration not only in vitro but also in vivo as a proof of concept. However, the EMA systems developed to date exist only as laboratory-scale experiments that do not take into account access to the patients, medical staff, and imaging devices. Moreover, the targeting test or therapeutic effect evaluation of microrobots is now limited to the in vitro or ex vivo test using a microscope or a camera because of the coil configuration and small workspace of the EMA system, which does not consider the in vivo environment. As a further issue, recent microrobot studies have focused on microrobot fabrication and magnetic targeting using the EMA system. However, without magnetic fixation, these microrobots can break off from the defect area because of the loose connection

[1]Korea Institute of Medical Microrobotics (KIMIRo), 43-26 Cheomdangwagi-ro, Buk-gu, Gwangju 61011, Korea. [2]School of Mechanical Engineering, Chonnam National University, 77 Yongbong-ro, Buk-gu, Gwangju 61186, Korea. [3]Biot Korea Inc., 43-26 Chemdangwagi-ro 208 Beon-gil, Gwangju 61001, Korea. [4]School of Biomedical Engineering, Xinxiang Medical University, Xinxiang, Henan 453003, China. [5]Center for Joint Disease, Chonnam National University Hwasun Hospital, 160 Ilsim-ri, Hwasun-eup, Hwasun 58128, Korea. [6]Department of Radiology, Chonnam National University Hwasun Hospital, 322 Hwasun-eup, Seoyang-ro, Hwasun 58128, Korea.
*These authors contributed equally to this work.
†Corresponding author. Email: seonbell@jnu.ac.kr (J.K.S.); jop@kimiro.re.kr (J.-O.P.); eunpyochoi@jnu.ac.kr (E.C.)

Downloaded from https://www.science.org at The Hong Kong University of Science and Technology (Guangzhou) on May 26, 2026

between MSCs on the microrobot and tissue of target lesion. Thus, after targeting of the microrobots using the EMA system, they must remain in the defect area for effective MSC delivery. Unfortunately, because of large volume and high power consumption of the EMA system, not only it is difficult to continuously generate magnetic fields but also this limits the movement of the patient. Therefore, to stably position microrobots in the defect area, a magnetic holding device arranged according to the position of the target lesion is needed. As a result, some drawbacks that do not account for such in vivo procedures slow the entry of microrobot systems into in vivo tests for cell-based therapies.

In our previous study, we demonstrated a proof of concept for a magnetic microrobot with the capability of targeted MSC delivery for articular cartilage regeneration (*14*). The microrobot, which was composed of a poly(lactic-*co*-glycolic acid) (PLGA) microscaffold containing polyethyleneimine (PEI)–coated magnetic nanoparticles (MNPs), has been known to disappear within a few weeks through hydrolysis of PLGA, but its degradation was not verified in the previous work. Also, the PEI-coated MNPs are not biodegradable and cause cell death and inhibition of cell (*17*). Although the biocompatibility of microrobot was verified, the PEI-coated MNPs remaining after the degradation of PLGA can affect surrounding cells and tissues. As a result, the PEI requires copolymerization with other monomers to facilitate its degradation (*17*). Therefore, the use of MNPs coated with noncytotoxic agents or verified in vivo is needed to proceed to the clinical stage of the microrobot. Next, for magnetic actuation of microrobot in 3D space, the EMA system, which is composed of eight electromagnetic coils, was introduced. The coil configuration of this EMA system has a radial structure such that eight coils are encircled in all directions. Although the motion of the microrobot can be observed in real time through a camera or microscope coupled with the EMA system, the EMA system was not compatible with the current medical imaging devices, such as an x-ray imaging device and an arthroscope, because it was not designed for in vivo applications. Therefore, the microrobot targeting test was limited on the knee joint phantom with small scale. In addition to the microrobot and the EMA system, conditions after targeting of the microrobot—such as stable fixation of microrobot in the target lesion, microrobot degradation, and cell survival—were not included in design, fabrication, and verification of the microrobot system. Thus, our previous study lacked understanding of cartilage regeneration and experimental preparation to validate the in vivo therapeutic effects of the microrobot system.

In this study, we propose a human adipose–derived MSC (hADMSC)–based medical microrobot system for knee cartilage regeneration and an in vivo trial to verify the efficacy of the microrobot using the cartilage defect model with consideration of clinical trial approval. This microrobot system can realize targeted MSC delivery containing minimally invasive procedures by needle-based injection, targeting, and fixation of the microrobot. As shown in Fig. 1, the microrobot system consists of (i) a magnetic microrobot for cell loading, (ii) an EMA system for targeted MSC transport of the microrobot, and (iii) a magnet for fixation of the microrobot according to clinical treatment procedures. The microrobot was prepared by adsorbing a magnetic microcluster on the surface of the PLGA microscaffold (step 1 in Fig. 1). A 3D porous microstructure of the microrobot supports the hADMSC, and it is injected into the joint cavity. Moreover, the magnetic microcluster, which was formed by the ionic charge interaction on the surface of the microrobot between ferumoxytol (Feraheme) and chitosan with negative and positive ionic charges, respectively, provides the magnetic actuation capability of the microrobot. Here, the ferumoxytol is a superparamagnetic iron oxide nanomedicine approved by the FDA as polyglucose sorbitol carboxymethyether–coated MNPs (*18*, *19*), and chitosan as a natural multifunctional polysaccharide is a representative cationic polymer that is biocompatible and degradable (*20*, *21*). The microrobot adsorbed by magnetic microclusters has stronger magnetic properties than the one of a previous study (*14*), and its degradation and viability, proliferation, and chondrogenic differentiation of hADMSC are ensured. To target the hADMSC-loaded microrobot (hADMSC-microrobot), an EMA system comprising six electromagnetic coils enables manipulation of the microrobot in 3D space (step 2 in Fig. 1). Furthermore, the coil configuration of the EMA system, which is designed for the minimum degrees of freedom (DOF) of the microrobot in vivo, allows access to the patient's knee, operator, arthroscope, and microrobot injection tool during an in vivo targeting procedure. In addition to targeting device of the microrobot, a single magnet was introduced to immobilize hADMSC-microrobots located at the defect after their targeting (step 3 in Fig. 1). The size and position of the magnet were optimized according to the location of the cartilage defect, and the magnetic field strength required microrobot delivery. Despite the externally applied force, secure fixation of the microrobots can be achieved using a strong magnetic field generated from the magnet. To verify the availability of the microrobot in an in vivo model, we prepared the microrobot-mediated MSC delivery system for the knee cartilage of small mammals. Resultantly, in vivo rabbit knee cartilage regeneration using this microrobot system could be demonstrated through the cell culture on the microrobot, cell delivery using the targeting device, and secure immobilization of cells using the fixation device. Synergistic effects between the microrobot, targeting, and fixation devices enhance the delivery of stem cell–based medicine and serve treatment capabilities that respond to the high targeting efficiency of stem cells.

RESULTS

Fabrication and characterization of the microrobot

The microrobot was fabricated by sequential formation of the PLGA microscaffold and the adsorption of a magnetic microcluster on its surface (step 1 in Fig. 1; see sections S1 and S2). First, the PLGA microscaffold was formed through a water-in-oil-in-water (w-o-w) emulsion–based gelatin leaching (*14*). As described in our previous study, the size and pore size of the PLGA microscaffold are determined by the injection rate of gelatin-in-PLGA (w-o) solution and the volume of the gelatin solution. The PLGA microscaffold has a spherical porous structure, which promotes cell penetration and nutrient exchange (fig. S1).

Subsequently, ferumoxytol, verified as safe in clinical applications by the FDA, was used in MNPs to provide magnetic actuation capability to the PLGA microscaffold. The small size (30 nm) (*18*, *19*) and high negative ionic charge of ferumoxytol provide high colloidal stability and safety for large-body doses; however, the limited surface area and strong negative ionic charge of the PLGA microscaffold interfere with the adsorption of ferumoxytol on its surface. Thus, biocompatible and biodegradable chitosan as a cationic polymer was used for the formation of magnetic microclusters [step 1 (i) in Fig. 1] to induce aggregation of MNPs for size increase and ionic charge change. The scanning electron microscopy (SEM) image of the

Downloaded from https://www.science.org at The Hong Kong University of Science and Technology (Guangzhou) on May 26, 2026

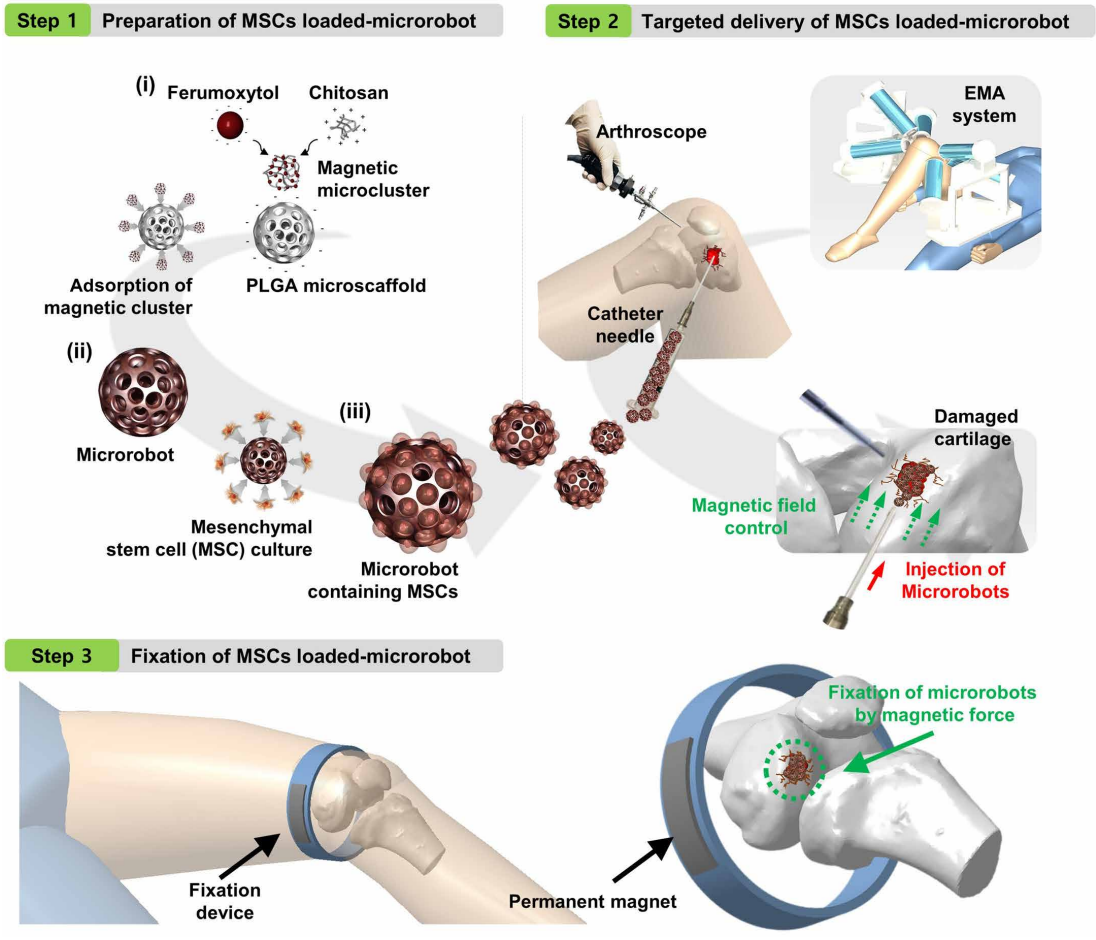

Fig. 1. Concept overview of knee cartilage regeneration procedures using magnetic microrobot-mediated MSC delivery system. The magnetic microrobot containing MSCs was prepared through a sequential process by adsorption of magnetic microclusters on the PLGA microscaffold and MSCs loading (step 1). The prepared MSC-loaded microrobots were delivered to cartilage defect using EMA system (step 2). After the targeted delivery procedure, the microrobots are immobilized to the defect using a permanent magnet (step 3).

magnetic microcluster shows magnetic aggregates formed by the ionic interaction between chitosan and ferumoxytol (Fig. 2A). The magnetic microcluster has an average size of 1.48 μm (Fig. 2B) and a weaker negative ionic charge (−13.17 mV) than ferumoxytol (−37.27 mV) (Fig. 2C). These results imply that the structural and surface properties of ferumoxytol were modified through the electrostatic interaction with chitosan.

As a final step in the fabrication of the microrobot, the prepared magnetic microcluster was adsorbed on the PLGA microscaffold [step 1 (ii) in Fig. 1]. The adsorption between these two substances is caused by the electrostatic interaction between the strong positive ionic charge of the chitosan of the magnetic microcluster and the negative ionic charge of the PLGA microscaffold (*21*). Moreover, other molecular interactions—such as hydrogen bonds, hydrophobic interactions, and van der Waals forces—aid the adsorption of magnetic microclusters on the PLGA microscaffold (*16*). In the SEM images (Fig. 2D), the microrobot exhibits little changes in size and pore compared with the PLGA microscaffold, regardless of the magnetic microcluster attachment. Energy-dispersive x-ray (EDX) spectrometry revealed the presence of the magnetic microcluster in the microrobot as C, O, and Fe signals were detected (Fig. 2E). Also, the overall scaffold and pore sizes of the microrobot measured by SEM images are 357.55 ± 18.57 μm and 43.85 ± 13.39 μm, respectively (Fig. 2F). The structural property of the microrobot satisfies the range of 100 to 500 μm and a pore size above 20 μm, which are conditions of the microscaffold to function as a cell carrier (*15*).

The chemical composition of the microrobot was analyzed by its infrared (IR) absorption band and thermal stability. Figure 2G shows the Fourier transform IR (FTIR) spectra for the microrobot and its constituent materials. The microrobot has major IR absorption bands of the magnetic microcluster and the PLGA microscaffold. Specifically, the $CONH_2$ absorption band near 1650 cm^{-1} indicates the presence of chitosan as a constituent of the magnetic microcluster (*22*). C—O—C stretching at 1650 cm^{-1}; C—O stretching between 1180 and 1085 cm^{-1}; and CH, CH_2, and CH_3 stretching vibrations between 2990 and 2850 cm^{-1} overlap with the chemical structure of the PLGA microscaffold (*23*). Furthermore, the peak near 630 and 550 cm^{-1} of the microrobot indicates the presence of γ-Fe_2O_3 (*24*). Similar peaks were also observed in ferumoxytol and the magnetic microcluster, confirming that ferumoxytol was composed of an iron oxide core of γ-Fe_2O_3. Next, the thermal stability of the microrobot was investigated using thermogravimetric analysis (TGA) with the

Downloaded from https://www.science.org at The Hong Kong University of Science and Technology (Guangzhou) on May 26, 2026

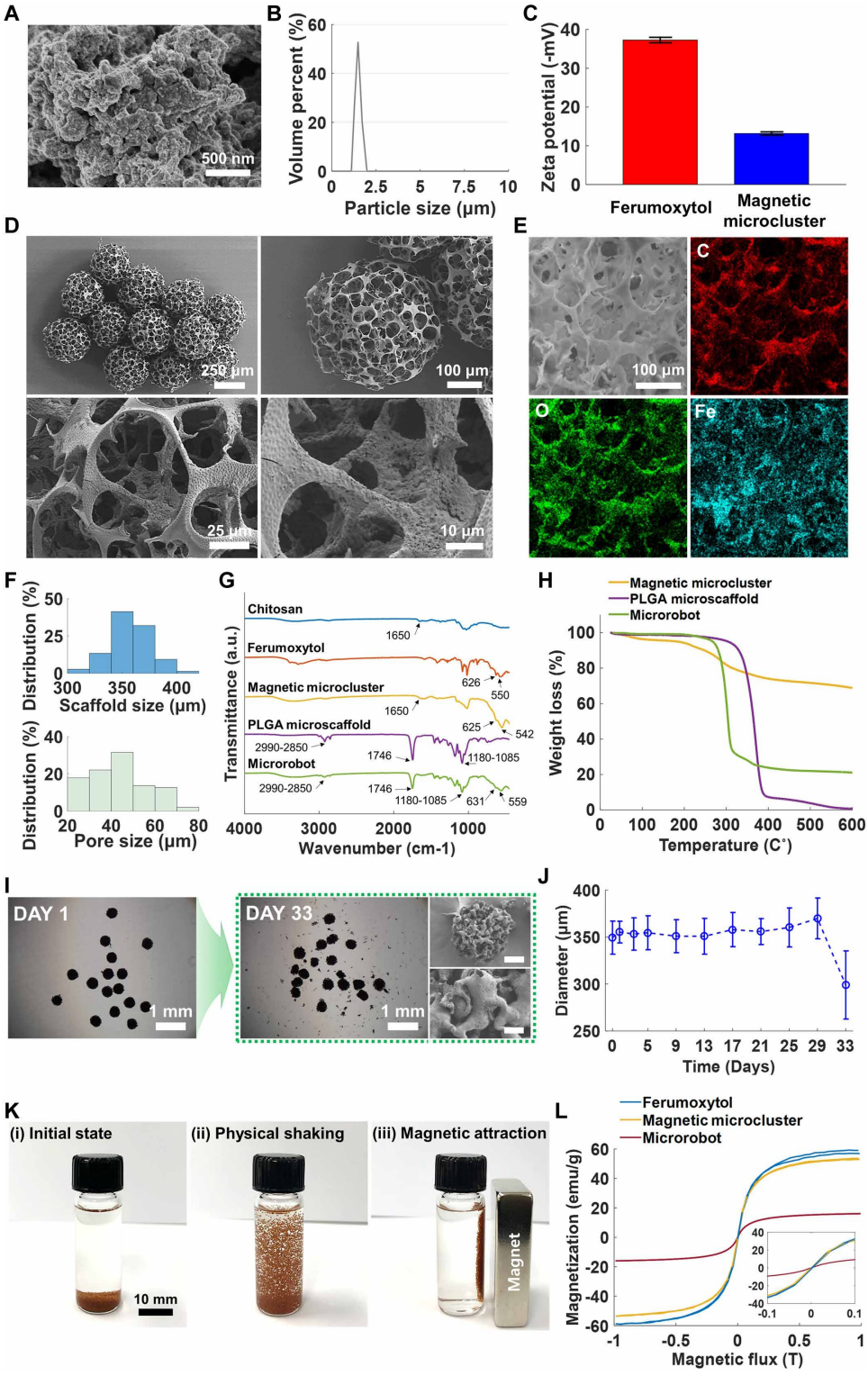

Fig. 2. Characterization of magnetic microrobot and microcluster. (**A**) SEM image of a magnetic microcluster. (**B**) Size distribution of magnetic microclusters in deionized water. (**C**) Zeta potential graph showing ionic surface charge of ferumoxytol and magnetic microparticle. (**D**) SEM images of magnetic microrobots. Top and bottom: Overall 3D porous structure and pore morphology of the microrobot, respectively. (**E**) EDX mapping of microrobot, which is mainly composed of carbon, oxygen, and iron. (**F**) Size distribution of microrobots and their pores. (**G**) FTIR spectra of chitosan, ferumoxytol, magnetic microcluster, PLGA microscaffold, and microrobot. a.u., arbitrary units. (**H**) TGA curves of magnetic microcluster, PLGA microscaffold, and microrobot. (**I**) Optical microscopy and SEM images of microrobots treated with lysozyme solution. On day 33, the scale bars of upper and lower SEM images are 100 and 20 μm, respectively. (**J**) Changes in diameter of microrobots with lysozyme solution with respect to time ($n > 13$). (**K**) Photographs showing responses of microrobots to physical shaking and magnetic attraction. (**L**) Magnetic hysteresis curves of ferumoxytol, magnetic microcluster, and microrobot measured by VSM.

PLGA microscaffold and magnetic microcluster (Fig. 2H). The weight of the PLGA microscaffold and magnetic microcluster decreases with increasing temperature, and this weight loss occurs rapidly at 250° to 400°C. At 600°C, the PLGA microscaffold is almost degraded, whereas the magnetic microcluster remains at 69% due to the decomposition of γ-Fe_2O_3 and chitosan main chains (*25*). On the basis of the residual amount of PLGA microscaffold and magnetic microcluster, the remaining 21% of the microrobot at 600°C represents the existence of a magnetic microcluster. Moreover, the high conductivity of γ-Fe_2O_3 in the microrobot facilitates the degradation of PLGA (*20*, *26*). These results indicate that the microrobot contains chitosan, ferumoxytol, and PLGA and maintains its chemical and physical properties.

As components of the microrobot, PLGA and chitosan are known to be degraded in vivo by hydrolysis and the lysozyme enzyme, respectively (*27*, *28*). Biodegradation of the microrobot was observed in phosphate-buffered saline (PBS) containing lysozyme after 33 days by observation through an optical microscope and an SEM (Fig. 2, I and J). The concentration of lysozyme was determined to be 120 μg ml^{-1} based on the synovial fluid at the knee joint with osteoarthritis (*29*). The shape of the microrobot was maintained on day 29 as compared with day 1, but its diameter was increased by about 5.84%. This phenomenon is caused by frequent PLGA swelling during degradation (*30*). On day 33, the microrobot shape collapsed because of significant degradation, and its residues were present in the lysozyme solution. Hence, the diameter of the microrobot decreased by about 14.45% during the incubation period.

Downloaded from https://www.science.org at The Hong Kong University of Science and Technology (Guangzhou) on May 26, 2026

Before the active targeting and fixation experiments of the microrobot, its magnetic properties were investigated under an external magnetic field through a magnetic actuation test and a magnetization curve. Figure 2I shows the magnetic actuation of microrobots using a permanent magnet. The microrobots located in the vial filled with PBS in the initial (i) and physical shaking (ii) conditions were either submerged on the floor or spread in the liquid. In contrast, when the magnet approached the microrobots, the microrobots moved quickly to the source of the external magnetic field (iii). Through the magnetic response of the microrobot by the magnet, we were able to predict the intensity and direction control of the magnetic field for precise targeting and secure fixation of the microrobot. Subsequently, the magnetic properties of the microrobot were quantitatively evaluated using a magnetization curve. As shown in Fig. 2J, the saturated magnetization of the magnetic microcluster decreased compared with ferumoxytol because of the binding between chitosan and ferumoxytol, in which the saturated magnetization of the microrobot is 16.01 electromagnetic unit (emu) g^{-1}. On the basis of these saturated magnetization values, the weight percentage of chitosan and ferumoxytol in the magnetic microcluster could be estimated to about 9.11 weight % (wt %) and 27.15 wt %, respectively. The saturated magnetization of the proposed microrobot is two times higher than the microrobot (8.09 emu g^{-1}) in our previous study (*14*). This difference in saturated magnetization means that the microsized magnetic aggregates are more adsorbed on the PLGA microscaffold than on the MNPs. Therefore, the driving force of the proposed microrobot under the same magnetic field strength is stronger than the one in our previous study. Moreover, the microrobot with the higher driving force can lead to the miniaturization of targeting and fixation devices.

hADMSC proliferation, adhesion, and differentiation in the microrobot in vitro

To investigate the effect of chitosan used for binding of ferumoxytol, which is one of the constituent materials of microrobots, we evaluated cell viability for cytotoxicity according to the treatment of ferumoxytol and the magnetic microcluster (ferumoxytol combined with chitosan). Ferumoxytol was reduced to 91% of the concentration of the control group at 32 to 64 μg ml^{-1}; however, the microcluster did not exhibit a significant decrease (Fig. 3A). The microrobot was fabricated using a microcluster in a concentration range that does not exhibit cytotoxicity, and the viability of the prepared hADMSC-microrobot [step 1 (iii) in Fig. 1] was evaluated. A cell spheroid was used as the control for evaluation, and cell viability was analyzed. There was no significant difference in cell viability between the PLGA microscaffold and microrobot compared with the control group (Fig. 3B). To determine the optimal loading condition of the microrobot according to the change of hADMSC loading time, we measured the efficiency of cell loading for 2 to 24 hours. As shown in Fig. 3C, the highest cell-loading efficiency was observed at 24 hours; however, no difference was observed at 2, 4, 6, and 12 hours, meaning that the microrobot can be applied through short-term loading. To confirm whether the microrobot was suitable for cell growth, we measured cell adhesion and proliferation rates by fluorescence staining and proliferation assay after cell loading on the microrobot, respectively. When the hADMSCs were incubated in the fabricated microrobot for 24 hours, it was confirmed that the loaded cells adhered harmoniously to the microrobot (Fig. 3D) and proliferated continuously until 16 days (Fig. 3E). Furthermore, there was no difference in cell proliferation between the two groups of the PLGA microscaffold and microrobot (Fig. 3E). This indicates that the microrobot fabricated under the prescribed conditions does not affect cytotoxicity and proliferation, and it is a suitable environment for cell growth.

To confirm that microrobot is suitable for cartilage regeneration, we cultured the hADMSC-microrobot for 21 days in chondrogenic differentiation induction medium. Subsequently, Alcian blue staining of the cartilage aggrecan (AGG) and expression of type II collagen (COLII) were used to evaluate differentiation potency. Consequently, it was confirmed that AGG and COLII were expressed on the microrobot exterior and interior (Fig. 3F and fig. S2). This implies that the hADMSC-microrobot successfully differentiates into chondrocytes and is suitable as a remedy for damaged cartilage regeneration. In addition, hADMSCs (undifferentiated cells), hADMSC spheroid, hADMSC-loaded PLGA (hADMSC-PLGA) microscaffold, and hADMSC-microrobot were evaluated for their ability to differentiate through comparison with cartilage-specific gene expression after differentiation into chondrocytes. The expression of cartilage-specific genes such as Sry-box 9 (*SOX9*), *COLII*, and *AGG* continuously increased with an induction period of cartilage differentiation for 7, 14, and 21 days. However, no significant difference in expression was observed between the three groups including hADMSC spheroid, hADMSC-PLGA microscaffold, and hADMSC-microrobot (Fig. 3G and fig. S3), indicating that the microrobot does not affect MSC differentiation.

Design and performance of the EMA system for microrobot targeting

A single electromagnetic coil or magnet can be applied to the microrobot targeting for knee cartilage repair. For example, defects located on the patellar articular surface can easily deliver MSC-loaded microrobots by placing a single magnetic source on the kneecap that generates magnetic forces in a direction perpendicular to the patella. However, the single magnetic source has difficulty delivering the microrobot to the medial and lateral condyle of the knee cartilage, an important defect site, because of limited accessibility of the device to the patient's knee. The limitation of microrobot targeting using this single magnetic source has been verified in the phantom considering the defect model of the patella (*31*, *32*) and medial condyle (*33*) of the rabbit knee joint (figs. S4 and S5 and movie S1). In the phantom mimicking the patella defect model, the magnet delivered the microrobot to the defect with a high targeting efficiency of 99.5 ± 1.45%, whereas the magnet showed a low microrobot targeting efficiency of 60.71 ± 18.39% in the medial condyle defect model. In particular, in the medial condyle defect model, the magnet's targeting efficiency is lower than only microrobot injection without magnet (76.0 ± 10.2%), and the microrobots in the defect are clustered in the direction of the magnet. These results indicate that the targeting accuracy of the microrobot is related to the direction of the magnetic field and the magnetic force formed by the defect. Therefore, the single magnet has a limitation in accurately delivering the microrobot in the defect of the medial condyle except for the patella.

On the other hand, the EMA system composed of multiple electromagnetic coils can generate a magnetic field in a desired direction of 3D space. Therefore, in this study, we introduced this EMA system as a microrobot targeting device for knee cartilage regeneration (step 2 in Fig. 1). The number and the arrangement of the electromagnetic coils of the EMA system were designed considering the manipulation area of the microrobot, the DOF according to the shape

Downloaded from https://www.science.org at The Hong Kong University of Science and Technology (Guangzhou) on May 26, 2026

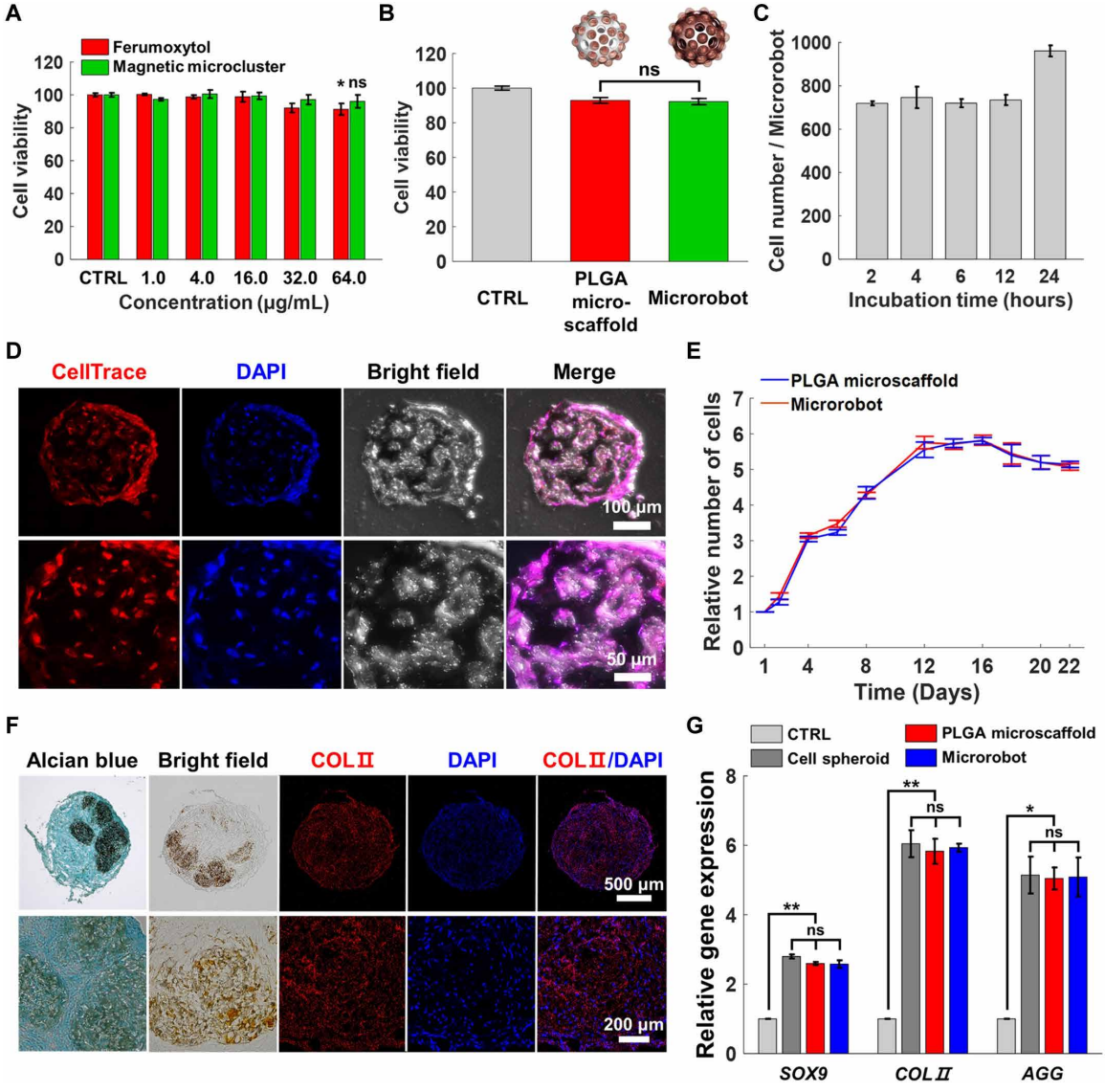

Fig. 3. Microrobots do not affect differentiation potency and provide a suitable environment for cell growth. (**A**) Evaluation of cytotoxicity after ferumoxytol (0 to 64 μg ml^{-1}) and magnetic microcluster treatment for 24 hours ($n = 3$; *$P < 0.05$, Student's t test). (**B**) Evaluation of cytotoxicity after cell culture in PLGA microscaffold and microrobot for 24 hours ($n = 4$). (**C**) Number of cells attached to the microrobot according to the incubation time after seeding 5000 cells into each microrobot. (**D**) Confocal images of hADMSC-microrobot, in which MSCs were incubated in the microrobot for 24 hours. Red and blue represent cytoplasmic and nuclear staining, respectively. (**E**) hADMSC proliferation in microrobot and PLGA-microscaffold for 1 to 22 days ($n = 3$). (**F**) Image of differentiated hADMSC-microrobot after culturing for 21 days in chondrogenic differentiation medium. Red and blue depict the expression of COLII and the nuclei, respectively. (**G**) Expression of cartilage-specific genes after 21 days ($n = 3$; *$P < 0.05$ and **$P < 0.01$, Student's t test).

of the microrobot, and the in vivo situation including the approach to the patient's knee, medical staff, and imaging devices. On the basis of the design parameters of the EMA system, the optimal coil configuration was obtained from an optimization routine, which forms all coil configurations and analyzes the workspace performance of each coil configuration. The optimal coil placement for knee cartilage regeneration is described in detail in the Supplementary Materials. Using the chosen coil configuration, the EMA system, which consists of six coils and a frame supporting them, was fabricated as shown in Fig. 4A and fig. S6. Imaging devices such as a camera, an optical microscope, and an arthroscope can be used with the EMA system. Detailed parameters of the EMA system are presented in tables S1 and S2. Before the magnetic manipulation test of the microrobot, the EMA system was characterized and calibrated through numerical simulation and measurement of the magnetic fields generated from the EMA system and a propulsion angle accuracy test of the magnetic object (see sections S4 and S5). Resultantly, the EMA system can simultaneously generate magnetic fields and gradients up to 80 mT and 1.2 T m^{-1} within 20 mm of the spherical workspace.

The mobility of the microrobot was evaluated according to magnetic fields, viscosity of a fluid, and cell loading. Figure 4B shows that the velocity of the microrobot in PBS increases proportionally by changing magnetic fields (10 to 40 mT, in increments of 10 mT)

Downloaded from https://www.science.org at The Hong Kong University of Science and Technology (Guangzhou) on May 26, 2026

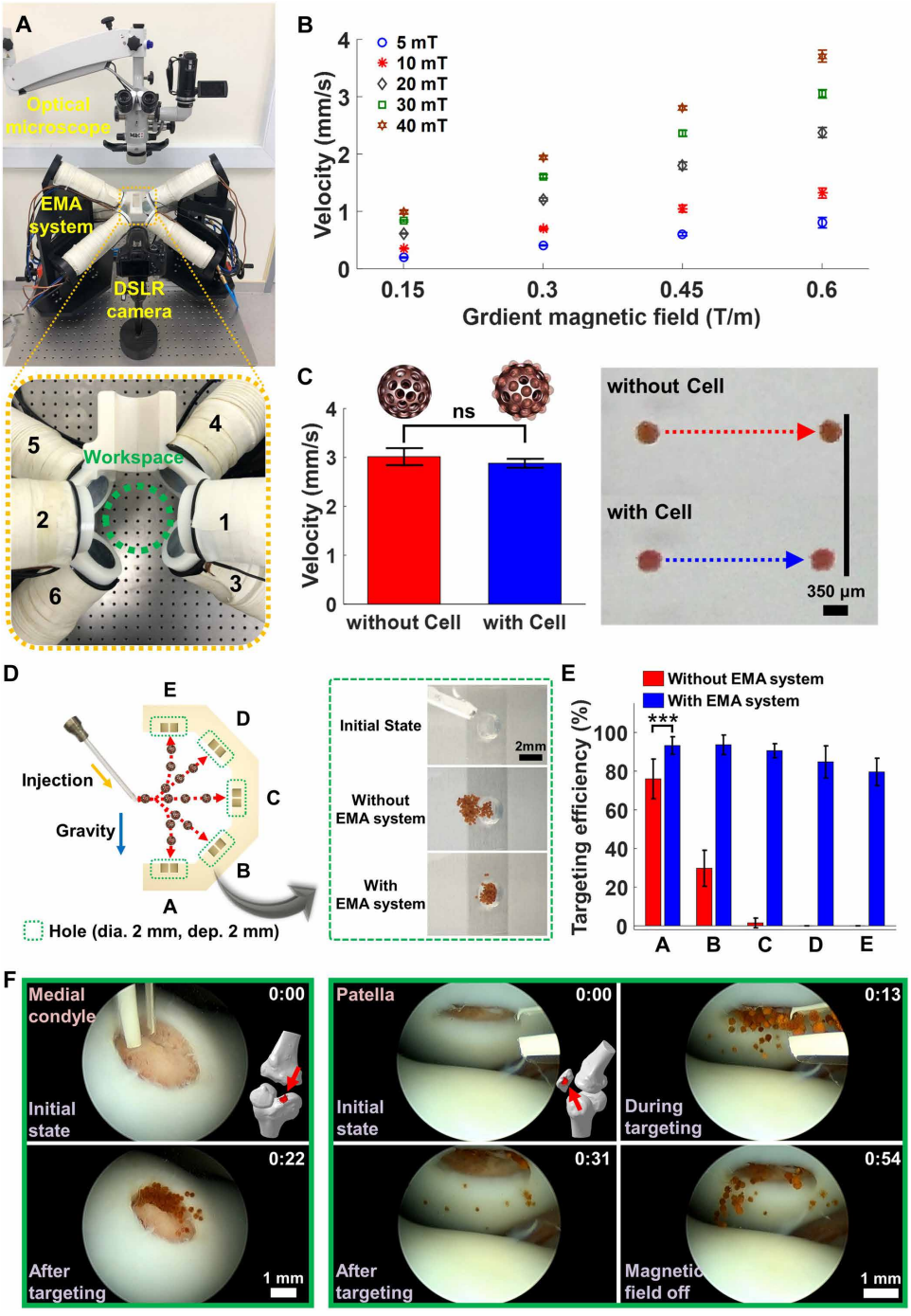

Fig. 4. EMA system with optimized coil figuration provides high targeting efficiency of microrobot. (**A**) Photograph showing the EMA system combined with imaging devices. (**B**) Mobility of microrobot at different magnetic fields and gradients ($n > 3$). (**C**) Mobility change of microrobot according to cell loading ($n = 4$). (**D**) Schematic diagram of a 3D targeting test in different phantoms (left). Screenshots of movies (right) show targeting of microrobot with and without EMA system at hole B. (**E**) Targeting efficiency of microrobots at each hole ($n > 5$; ***$P < 0.001$, Student's *t* test). (**F**) Time-lapse image sequence of microrobots during targeting at defect of medial condyle (left) and patella (right) in ex vivo porcine knee. In each image, the red arrows in knee joint model indicate the defect position. The time is indicated on each image in the minutes:seconds format.

and the gradient (0.15 to 0.60 T m^{-1}, in increments of 0.15 T m^{-1}), where the PBS is filled by an arthroscope system before surgery to ensure visualization and removal of debris. The mobility of the microrobot is caused by the linear change of its magnetization under the magnetic field and the gradient range generated from the EMA system. Although PBS replaces the synovial fluid known to have high viscosity through the arthroscopic system, residual synovial fluid may affect the movement of the microrobot. Thus, we measured the velocity of the microrobot in glycerol solutions [50, 60, 70, 75, and 80% (v/v)] with different viscosity values (6.63, 12.97, 25.07, 38.83, and 62.30 cP). The viscosity of these glycerol solutions is similar to that of inflamed synovial fluid with a viscosity of 20 cP or higher (*34*, *35*). As shown in fig. S7, under a constant magnetic field (30 mT) and gradient (0.60 T m^{-1}), the velocity of the microrobot decreased with increasing glycerol concentration. The result indicates that the magnetic driving of the microrobot is greatly affected by the viscosity of the fluid. Furthermore, the mobility change by hADMSC loading on the microrobot was observed in PBS under a constant magnetic field (30 mT) and gradient (0.60 T m^{-1}) (Fig. 4C). The average velocity of the hADMSC-microrobot is 2.88 mm s^{-1}, which is slightly slower than before cell loading (average, 3.01 mm s^{-1}). The difference of velocity is less than ~4.4%, and it is caused by cell weight and the release of the magnetic microcluster loosely attached to the microrobot during the cell culture.

On the basis of the magnetic driving performance of the microrobot, the 3D manipulation of the microrobots was tested in a knee joint phantom with a defect in the medial condyle (movie S2). The swarm motion of the microrobots showed fast and precise targeting. However, in the clinical test, it is not easy to move hundreds to thousands of microrobots injected through a needle with narrow diameter simultaneously to the defect in a small joint space. Therefore, for practical targeting of the microrobot in the knee joint cavity, the needle is located close to the defect, and the microrobots injected through this needle move directly to the defect along the magnetic field generated by the EMA system. To verify the targeting technique, the 3D targeting test of microrobots was conducted in different phantoms with a hole at five points (A, B, C, D, and E) (Fig. 4D and movie S3). One hundred microrobots were injected near the defect through a 16-gauge catheter needle and guided to each hole using the magnetic field

Downloaded from https://www.science.org at The Hong Kong University of Science and Technology (Guangzhou) on May 26, 2026

control of the EMA system. In the case without magnetic targeting, microrobots were positioned at holes A, B, and C by gravity, and the average targeting efficiency at each hole was 76, 29, and 1.5%, respectively (Fig. 4E). Despite the effect of gravity, the low targeting effect is attributed by fluid vortex formation upon microrobot injection. The fluid flow formed in the hole and surroundings of the microrobot injection was confirmed by numerical simulation (fig. S8). As a result, the fluid flow by microrobot injection hits the wall of the hole and is directed out of the defect. These simulation results explain the phenomenon of low targeting efficiency when microrobots are injected as defects without the aid of magnetic fields. It was challenging to move the microrobot, which must overcome gravity, to holes D and E; hence, the microrobots sank to the bottom simultaneously with the injection. In contrast, when magnetic targeting using the EMA system was applied, at least 80% of the microrobots were located at the defect (Fig. 4E). The targeting error is caused by manual manipulation of the catheter needle position and the microrobot injection rate by the operator. Despite this target error, we found that the magnetic guidance of the microrobot by the EMA system showed a marked increase of targeting efficiency in comparison with the microrobot injection by itself.

To confirm the feasibility of the EMA system in the in vivo application, we performed an ex vivo targeting test using an arthroscope system on the porcine knee (movie S4). The medial condyle and patella, which have a defect of 4 mm in diameter, were designated as the target site of the microrobot. First, in the medial condyle, most of the 100 microrobots were placed at the defect with the help of the magnetic field and gravity (Fig. 4F, left). Conversely, without the help of magnetic fields, the microrobots floated in the joint space, and only a few reached the defect site (fig. S9, left). This phenomenon is caused by the fluid flow generated as the PBS injected with the microrobot strikes the defect surface. Subsequently, in the patella, a large number of microrobots overcame gravity and traveled to the defect along the magnetic fields generated by the EMA system (Fig. 4F, right). After targeting, when the magnetic field generation of the EMA system was shut off, the microrobots fell away from the defect. This result indicates the need for microrobot fixation after its targeting. In contrast, with microrobot injection only, all microrobots were sprayed across the joint cavity because of the gravity effect (fig. S9, right). As a result, we confirmed that the ex vivo targeting test results are similar to those of the 3D targeting test of microrobots and that microrobot targeting using the EMA system can be used in knee cartilage regeneration.

Placement and performance of a magnet for fixation of microrobot

After magnetic targeting of the microrobot using the EMA system, a single magnet was used as a fixation tool to wear on the rabbit knee (step 3 in Fig. 1). Although a microrobot fixation device consisting of a single permanent magnet is not suitable for use during the microrobot targeting process, it can serve to fix the microrobot to cartilage defects after its targeting. More specifically, unlike microrobot targeting, which requires precise magnetic field direction control, microrobot fixation located in a defect does not require as much magnetic field orientation precision as the targeting. Therefore, to stably fix the microrobot located in the defect, the magnetic field from the magnetic fixation device needs to be generated inside the defect, but some magnetic field error is allowed.

In this work, we chose the medial condyle as a lesion for stably fixing the microrobot from the patellar articular surface, and the medial condyle is where cartilage defects frequently occur. Briefly, defects located on the patellar articular surface can easily fix the microrobot by placing a magnet on the kneecap that generates magnetic forces in a direction perpendicular to the patella (fig. S10A). To verify the fixation of the microrobot with the magnet in the patella defects, we performed numerical simulations, where the magnet position and defect region were determined by referring to the thickness and the width of the rabbit patella, respectively (*31*, *32*). As a result, the magnetic fields and force maps showed that both the magnetic field and the magnetic force generated from the magnet are directed into the defect (fig. S10B), which means that the microrobot can be fixed in the defect. Furthermore, we performed a microrobot targeting test in phantoms that mimic the patella defect model (figs. S4 and S5 and movie S1). The targeting test, not a fixation test, showed that the magnet in patella defects not only has a high targeting efficiency of 99.5 ± 1.45% but also overcomes the fluid vortex formed by microrobot injection.

Unlike the patella defects, the defects in the medial condyle are located perpendicular to the femur. To fix microrobots targeted to the defect in the medial condyle, a magnetic force orthogonal to the femur needs to be formed to face the defect. Recently, several research groups introduced magnet implantation into the subchondral bone of the medial condyle, and as a result, the MNP-loaded stem cell or stem cell–loaded magnetic scaffold was stably fixed inside the defect (*36*, *37*). However, during implantation of the magnetic source, the surface coating of the implant is able to be peeled off and may cause toxicity due to the corrosion of the implant. Also, because the magnet implantation requires invasive surgery of drilling and wide incision to the subchondral bone, this method leads to a longer patient recovery period. To fix the microrobot in the defects of the medial condyle while avoiding the implantation of these magnetic sources, the magnet can be attached to the skin of the knee joint in the tibia (fig. S11) and distal femur (Fig. 5A). When the magnet was placed in the tibia, we confirmed by numerical simulation that the direction of the magnetic force caused by the magnet occurred outside the defects of the medial condyle (fig. S11). In addition, because the medial condyle defects are located in the distal femur, bending of the knee joint causes a change in the position of the magnet and the direction of the magnetic fields. Thus, the microrobots delivered by the EMA system can easily escape from the defect. On the other hand, because the magnet located in the distal femur is located in the same bone as the medial condyle defect, the magnet position change due to the motion of the knee joint can be minimized (Fig. 5A). Moreover, the magnetic field and magnetic force maps through numerical simulations show that the direction of the magnetic force from the magnet occurs inside the defect of the medial condyle.

To apply the single magnet to a defect model of the rabbit knee joint, we determined the placement of the magnet to be attached to the distal femur outside the leg, considering the defect position in the medial condyle of the rabbit and the posture of a usual sitting rabbit (*33*). Moreover, because of the skin and muscle motions as well as magnet attachment errors, we set up the region where the defect can be located by the attachment of the magnet (Fig. 5A). The desired region of the defect had the dimensions of width by length by height of 5 mm by 20 mm by 10 mm, respectively, and the center of the region was 17.5 mm and 5 mm away from the center of the magnet surface in the x- and z-axis directions, respectively.

Downloaded from https://www.science.org at The Hong Kong University of Science and Technology (Guangzhou) on May 26, 2026

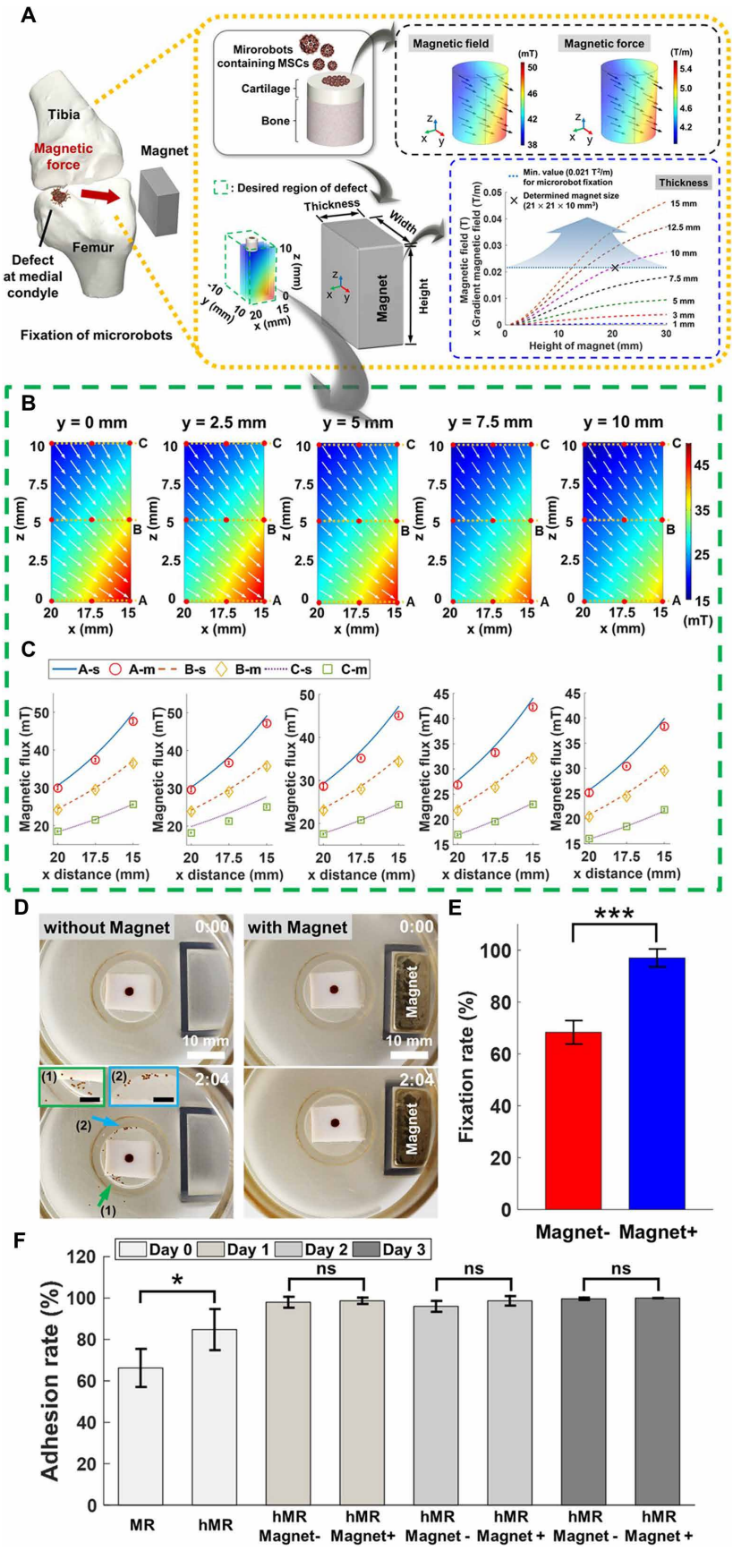

Fig. 5. Magnet enhancing MSC transport to cartilage defect through magnetic fixation of microrobots. (**A**) Schematic illustration of magnet placement on rabbit knee joint. Magnetic fields and gradient maps inside black dashed-line box indicate numerical simulation results of cartilage defect. The graph inside blue dashed-line box shows optimization of magnet size. (**B**) Numerical simulation results of magnetic fields generated from a magnet within defect region. In each magnetic field map, three red points on dotted lines (A, B, and C) were used for comparison of measured and simulated magnetic fields. (**C**) Simulated (A-s, B-s, and C-s) and measured (A-m, B-m, and C-m) magnetic fields at 45 positions within the defect region. (**D**) Time-lapse images of microrobot fixation test performed without and with the magnet. Areas near the numbered arrows are enlarged in the insets. Scale bars, 3 mm. Time is indicated on each image in the minutes:seconds format. (**E**) Fixation rates of microrobots without (−) and with (+) the magnet ($n = 3$; $^{***}P < 0.001$, Student's t test). (**F**) Adhesion rates of microrobots according to cell loading, use of magnet, and cell culture day ($n = 3$; $^{*}P < 0.05$, Student's t test). MR, microrobot; hMR, hADMSC-microrobot; ns, not significant.

Furthermore, the magnet size (21 mm by 21 mm by 10 mm for width by length by thickness, respectively) was determined by considering the size of the rabbit medial condyle and the intensity of the gradient and magnetic fields. In more detail, the width of the magnet was chosen through the medial anteroposterior diameter of the rabbit (about 20 mm) (*33*). The height and thickness of the magnet were selected on the basis of the intensity of the gradient and magnetic fields (35 mT and 0.6 T m^{-1}, respectively) of the EMA system used for in vivo targeting of the microrobot (a graph inside blue dashed-line box in Fig. 5A).

We analyzed the magnetic field and gradient generated from the magnet within the defect region by numerical simulation. As shown in Fig. 5B and fig. S12, the magnetic field and gradient were stronger toward the center of the magnet and had the maximum intensity of 49.82 mT and 5.65 T m^{-1} and a minimum of 15.89 mT and 1.42 T m^{-1}, respectively. Because the magnetic field gradient acting on the z axis (maximum and minimum angles of −68.30° and −20.67° from the xy plane) is directed into the defect, microrobots located at the defect could be stably fixed. Furthermore, we measured the magnetic field generated from the magnet at 45 positions and compared it with the simulation results (Fig. 5C). The magnetic fields measured at all positions were not significantly different from the simulation result, and a discrepancy of 1.92% occurred between the two results. The error was caused by the misalignment of the magnet and the residual magnetism of the class of neodymium magnet.

The feasibility of microrobot fixation was verified by phantom experiments using an ex vivo porcine cartilage sample with a defect of 2 mm diameter and 2 mm depth. As an external force to confirm microrobot fixation, physical shaking was applied to 100 microrobots located inside the defect for 2 min at 50 rpm. As shown in Fig. 5D and movie S5, a large number of microrobots exited the defect area because of external shaking (Fig. 5D, left), whereas magnetic fixation with

Downloaded from https://www.science.org at The Hong Kong University of Science and Technology (Guangzhou) on May 26, 2026

the magnet kept almost microrobots inside the defect (Fig. 5D, right). The fixation rate of the microrobot without and with the magnet was 68 and 97%, respectively (Fig. 5E). More than half of the microrobots were located inside the defect, even though magnetic fixation using the magnet was not applied. As a component of the magnetic microcluster on the surface of the microrobot, chitosan has a unique tissue adhesion property because of its polycation properties (*38*). Hence, it is hypothesized that this phenomenon is caused by adhesion between the microrobot and cartilage tissue of the ex vivo sample. In addition, the patient's weight-bearing activity is limited after the cell-based therapy (*39*), and the flow of about 4 ml of the synovial fluid with a replacement cycle per day is very slow (*40*, *41*). Therefore, the demonstration of the stable fixation of the microrobot at physical shaking of 50 rpm, faster than the human walking stroke frequency (30 rpm) (*42*), indicates that the proposed magnet placement and performance could be applied in an in vivo defect model.

To determine the wearing period of the magnet after targeting of the microrobot, we performed an adhesion test of the microrobot on cartilage tissue. One hundred hADMSC-microrobots were located in the defect of the ex vivo porcine cartilage sample, and adhesion of the microrobots was observed at days 0, 1, 2, and 3, depending on the presence or absence of the magnet. As shown in Fig. 5F and movie S6, at day 0, the adhesion of hADMSC-microrobot is about 18.5% higher than using microrobot alone. The high adhesion effect of the hADMSC-microrobot is a result of helping cells interact with the tissue of the ex vivo sample (*43*, *44*). Since day 1, most hADMSC-microrobots, regardless of the magnetic fixation, did not fall out of the defect. These results imply that the hADMSCs on the microrobot are sufficiently connected to the tissues around the defect. Thus, in our in vivo test, the magnet was worn for 1 day after targeting of the hADMSC-microrobot.

In vivo validation of cartilage regeneration using a microrobot system

In vivo cartilage regeneration was performed in a rabbit knee using the proposed microrobot system, followed by incubation of hADMSCs on the microrobot and targeting and fixation of the hADMSC-microrobot. In the targeting step of the hADMSC-microrobot (Fig. 6A, top), the rabbit knee joint, which has a defect in the medial condyle, was positioned in the workspace of the EMA system, and the hADMSC-microrobot was delivered through open surgery due to the narrow joint space. Before the in vivo cartilage regeneration test, targeting of the hADMSC-microrobot in open surgery was observed in the ex vivo rabbit knee (movie S7). The only hADMSC-microrobot injection, despite the help of gravity, had a low targeting efficiency because of the flow of PBS injected with hADMSC-microrobots. In contrast, magnetic targeting using the EMA system allowed most hADMSC-microrobots to move to the defect. This result shows that magnetic targeting using the EMA system could be applied not only in the fluid but also in the air-filled environment in the joint space. Subsequently, in the fixation step of the hADMSC-microrobot (Fig. 6A, bottom), one magnet was attached to the outer femur of the rabbit knee using a double-sided tape based on the defect region, and the self-adherent wrap was surrounded by the legs and waist of the rabbit to prevent the magnet from escaping.

After these steps, targeting and fixation effects of hADMSC-microrobots in rabbit knee cartilage were investigated through gross observation of the knee cartilage with the defect after targeting and 1 week later. As shown in Fig. 6B, most of the hADMSC-microrobots were located in the defects in the case of targeting using the EMA system and fixation using the magnet. However, in the absence of targeting and fixation, a few of hADMSC-microrobots were present in the defect, and the rest were found in the synovium membrane and other tissues (see arrows and enlarged images in Fig. 6B).

To verify the suitability of the hADMSC-microrobot as a therapeutic agent for cartilage regeneration, first, we measured the period of biodegradation of hADMSC-microrobot transferred to the lesion site in vivo using the EMA system. The hADMSC-microrobot injected into the lesion was observed at 1 to 3 weeks, and the degradation of microrobot was observed by gross observation and Prussian blue iron staining. When the results of each period were compared, it was observed that the hADMSC-microrobot engrafted in the lesion site degraded over time (Fig. 6C). Moreover, the magnetic microcluster, one of the components of the microrobot, was not separated from the microrobot at the first week; however, after 2 to 3 weeks, it was observed to be separated from the microrobot and distributed to the articular cartilage of the femoral condyle, along with a gradual decrease (Fig. 6C). Compared with the in vitro decomposition of microrobots, rapid degradation of microrobots in an in vivo environment is expected to occur with periodic replacement of body fluids. Because the hADMSC-microrobot was degraded in the cartilage, the biodistribution of cells was confirmed by CellTrace and 4′,6-diamidino-2-phenylindole (DAPI) staining to confirm the engraftment of hADMSC injected into the lesion in cartilage of the femoral condyle. When the cartilage distribution of cells injected at the first week and 3 weeks after injection was confirmed, it was observed that the injected cells gradually increased for 3 weeks in the articular cartilage of femoral condyle (Fig. 6D and fig. S13). This indicates that the hADMSC-microrobot located in the lesion was degraded in 3 weeks and that the hADMSCs carried on the microrobot did not disappear with the degradation of microrobot but were implanted on the cartilage lesion site. Hence, to confirm the inflammatory response due to degradation of the microrobot, we confirmed expression of acute inflammatory–related genes such as *IL1*β, *IL-6*, *TNF-α*, and *IL-8* in the rabbit synovium, synovial fluid, lymph node, and spleen at 3 weeks after injection of the microrobot. The expression of *IL1*β, *IL-6*, *TNF-α*, and *IL-8* in all isolated tissues was not significantly different between the hADMSC-PLGA microscaffold and the hADMSC-microrobot when compared with the control group (Fig. 6E), meaning that the microrobot does not stimulate the expression of proinflammatory genes that cause inflammation.

Cartilage regeneration in the noninjected group (defect) and the hADMSC-microrobot–injected group [with microrobot system (wMS) and without microrobot system (woMS)] was analyzed through hematoxylin and eosin (H&E) and COLII staining to confirm the effect of cartilage regeneration by the microrobot system. The expression of COLII significantly increased in the hADMSC-microrobot–injected group compared with the noninjected group at 2 and 3 weeks after injection, and we observed a significant increase in the COLII expression in the wMS group compared with the woMS group (Fig. 6, F and G, and fig. S14). This means that the microrobot system improved the cartilage regeneration effect by enhancing the delivery of the hADMSC-microrobot.

DISCUSSION

We proposed a magnetic microrobot-mediated MSC delivery system to improve the absence of active targeting of cells in the knee

Downloaded from https://www.science.org at The Hong Kong University of Science and Technology (Guangzhou) on May 26, 2026

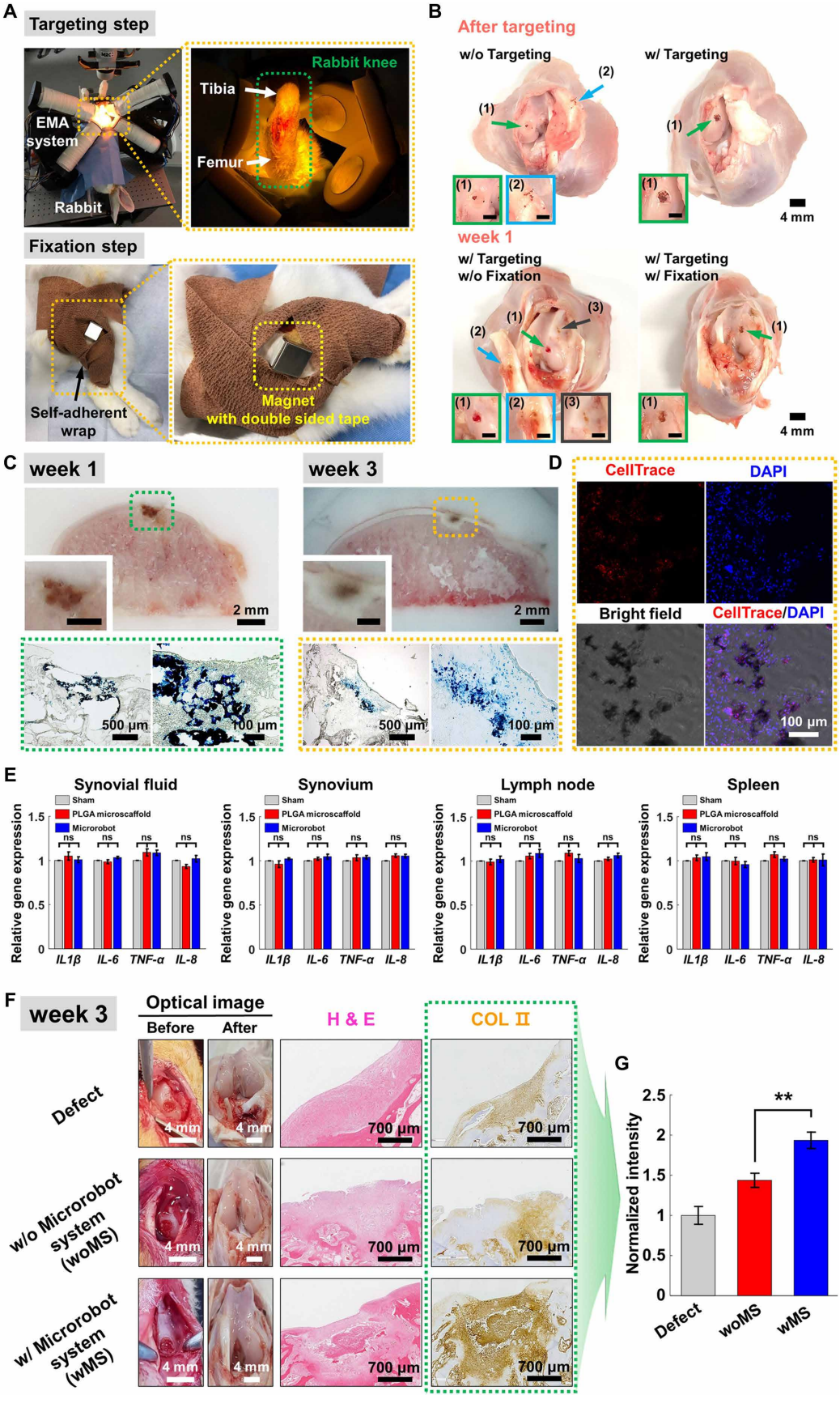

Fig. 6. In vivo cartilage regeneration using magnetic microrobot-mediated MSC delivery system. (**A**) Images of EMA system and magnet applied to rabbit knee in targeting (top) and fixation (bottom) steps. (**B**) Macroscopic appearances of microrobots after magnetic targeting (top) and 1 week after magnetic fixation (bottom). Areas near the numbered arrows are displayed in the insets. Scale bars, 2 mm. (**C**) Image of gross (top) and Prussian blue staining (bottom) at the first week and 3 weeks after hADMSC-microrobot injection. The green (left) and yellow (right) dotted squares represent the Prussian blue iron staining area at the first week and 3 weeks, respectively. (**D**) Fluorescence image of engrafted cells present in cartilage using CellTrace (red) 3 weeks after hADMSC-microrobot injection. DAPI (blue) was used for counterstaining of CellTrace. (**E**) Expression of inflammatory genes *IL1*β, *IL-6*, *TNF-*α, and *IL-8* in tissue isolated from inflammatory response and regulatory organs after microrobot injection ($n = 4$). (**F**) H&E and COLII staining of the cartilage tissue in defect group (top) and microrobot system group (w/o, middle; w/, bottom) at 3 weeks. (**G**) COLII expression quantified by ImageJ software ($n = 3$; $^{**}P < 0.01$, Student's *t* test).

cartilage regeneration. The microrobot system consists of a magnetic microrobot body capable of supporting MSCs, an EMA system for 3D microrobot targeting to the damaged cartilage, and a magnet for fixation of the microrobot. Each component was verified by in vitro and ex vivo tests, and subsequently, the in vivo cartilage regeneration was performed using the proposed microrobot system in the defect model of the rabbit knee cartilage. Hence, the hADMSC-microrobots were targeted and fixed to the defect using the EMA system and magnet, and no inflammation reaction was found at this time. The microrobot located in the defect was slowly degraded, and the MSCs persisted without apoptosis. The hADMSC-microrobot using the EMA system and the magnet showed a cartilage regeneration effect compared with other experimental groups.

Downloaded from https://www.science.org at The Hong Kong University of Science and Technology (Guangzhou) on May 26, 2026

The microrobot was fabricated as a combination of the PLGA microscaffold and magnetic microcluster (ferumoxytol combined with chitosan). The degradation of the PLGA microscaffold into lactic and glycolic acid was reported, and the pH change was controlled according to their composition ratio (*27*). The microrobot was degraded in vitro and in vivo for about 3 weeks. The acidic properties of PLGA degradation can cause damage to the cartilage tissue (*45*); however, the microrobot did not cause any inflammation or damage to cartilage tissue and organ. This indicates that the microrobot is a suitable material for stem cell delivery for cartilage regeneration.

Ferumoxytol, which is one of the components of the microrobot used in this study, has been used as a therapeutic agent for contrast media and iron deficiency treatment (*18*, *19*). Ferumoxytol is used at a dose of 510 mg when used as a treatment for iron deficiency, and it is used in a concentration range of 1 to 6 mg kg^{-1} when used as a contrast media. In this study, the concentration of ferumoxytol used in the microrobot for cartilage regeneration is in the range of micrograms. In addition, ferumoxytol is mainly distributed in the mononuclear phagocyte system organs, such as the liver and spleen, and has a relatively low distribution in the lung, heart, and kidney (*46*). The ferumoxytol binds to hemoglobin via plasma transferrin, is distributed in Kupffer cells in the liver, and is removed through phagocytosis of the macrophage in the reticuloendothelial system (*47*). In this study, ferumoxytol used in the microrobot did not exhibit cytotoxicity, proliferation, differentiation, and inflammatory response when applied at the microgram concentration, and it is hence a polymer suitable for the microrobot stem cell delivery for cartilage regeneration.

In clinical trials, stem cells were transplanted at 1×10^6 to 2.5×10^6 cells cm^{-2} in the lesion site, and in preclinical studies for clinical entry, 8×10^5 to 1×10^7 cells cm^{-2} were used for cartilage regeneration (*1*). The microrobot presented in this study is a system for delivering the hADMSC-microrobot to a lesion site through a noninvasive method using the EMA system. For this reason, the loading efficiency of hADMSC on the microrobot and cell proliferation are important factors. As shown in Fig. 3C, when the loading efficiency was observed from 2 to 24 hours, the cell-loading efficiency up to 12 hours did not show a significant difference, meaning that a sufficient number of cells for clinical application can be loaded on a microrobot in a short time. Moreover, the hADMSCs were observed to proliferate continuously in the microrobot, and the proliferation was observed to decrease with the degradation of the microrobot (Fig. 3E). During the degradation of the microrobot, the loaded hADMSCs migrated to the cartilage lesion site and were observed to engraft in the tissue (Fig. 6D). In the current study, 100 microrobots injected into the rabbit knee joint cartilage were capable of delivering about 8×10^4 cells in a short time (4 hours). The number of cells is significantly lower when compared with previous preclinical studies; however, most cells are lost without reaching the lesion site in a typical cell injection method (*1*). Moreover, only a few stem cells among the transplanted cells are differentiated into chondrocytes. This indicates that it is very important to improve the efficiency of delivery of the cells to the lesion site to improve their therapeutic utility. In the present study, the cells were efficiently delivered to the lesion site using the microrobot system (Fig. 6B), and the delivered stem cells efficiently regenerated the cartilage (Fig. 6, F and G). Furthermore, the microrobot system enables minimally invasive cartilage regeneration, which allows for rapid recovery of the patient and a favorable prognosis, unlike the conventional invasive cartilage regeneration technique. Thus, the use of the microrobot system indicates that a lower number of stem cells harvested through the short-term culture can be efficiently applied in clinical trials for cartilage regeneration.

Although the proposed stem cell–mediated microrobot system has been shown to be applicable to in vivo cartilage regeneration, some technical issues need to be improved or developed to be applied to future clinical tests. First, a microrobot injection device needs to be developed to stably inject a cell-loaded microrobot. In this study, microrobots were manually injected through a 16-gauge needle, resulting in microrobot targeting errors due to irregular injection rates. Therefore, we expect that the use of microrobot injection device will improve the targeting effect of microrobot. Next, in this study, without a complex structure, one magnet was used for microrobot fixation due to the small size of the rabbit joint. Unlike rabbits, where the magnet is located outside the femur due to continuous joint motion and posture, human joint motion can be minimized under the medical staff's control. Therefore, the area where the magnet can be attached to the human knee joint is wider than that in a rabbit. In addition, we expect to be able to hold the microrobot to various defects of the knee joint by applying a magnet array that can generate a magnetic field in the desired intensity and direction at various positions of the knee joint. Last, the safety of the proposed cell-loaded microrobot needs to be evaluated for a long time through the in vivo test, and in addition, knee cartilage regeneration using the microrobot system should be performed in large animals with similar knee joints to the human. We are planning an in vivo test for long-term evaluation of cartilage regeneration using the microrobot system. Also, we will build a microrobot system for human knee cartilage regeneration, where targeting and fixation devices will be made to keep their size small while maintaining their current functionality.

MATERIALS AND METHODS

Detailed fabrication of the microrobot is presented in sections S1 and S2. In addition, detailed in vitro, ex vivo, and in vivo tests are explained in sections S8 to S14.

Characterization of the magnetic microcluster and the microrobot

Ionic surface charge and size distribution of the magnetic microcluster were measured by the surface zeta potential and the particle size analyzer (ELS-8000, Otsuka, Japan). Morphologies of the magnetic microcluster and the microrobot were observed using a SEM (SU8010, Hitachi, Japan). C, O, and Fe signals of the microrobot were detected using EDX. The diameter of the microrobot and their pore sizes were measured using ImageJ software (National Institutes of Health, USA). TGA for three samples (magnetic microcluster, PLGA microscaffold, and microrobot) was carried out using a TG 209 F1 (NETZSCH Instruments Co. Ltd., Germany) thermal gravimetric analyzer at a heating rate of 20°C min^{-1} under N_2 atmosphere. FTIR spectra of five samples (chitosan, ferumoxytol, magnetic microcluster, PLGA microscaffold, and microrobot) were recorded on a Nicolet Nexus 670 FTIR spectrophotometer (Thermo Nicolet Corporation, USA) with 16 scans per sample ranging from 400 to 4000 cm^{-1} and a resolution of 4 cm^{-1}. The magnetic hysteresis curve of three samples (ferumoxytol, magnetic microcluster, and

Downloaded from https://www.science.org at The Hong Kong University of Science and Technology (Guangzhou) on May 26, 2026

microrobot) was obtained using a vibrating sample magnetometer (VSM; Lake Shore Cryotronics 7404, USA).

Degradation of the microrobot

Microrobots were incubated in PBS with lysozyme (120 μg ml^{-1}) at 37°C under agitation (60 rpm). Degradation of the microrobot was monitored for 33 days, with daily replacement of the lysozyme solution. The morphology of the microrobots was observed using a Nikon Eclipse Ti-E inverted microscope and a SEM. The diameter of the microrobots was measured from the microscopy image using ImageJ software.

Characteristics of primary hADMSCs and cell culture

hADMSCs were purchased from ScienCell Research Laboratories Inc. (USA). The cells were tested for viral infection and mycoplasma contamination and presented all negative results. Cell phenotypes analyzed by flow cytometry showed $CD73^+$, $CD105^+$, and $CD31^-$. The hADMSCs were cultured in T175 flasks (Corning, USA) according to the manufacturer's recommendations. Cells were cultivated in Dulbecco's modified Eagle's medium (Gibco, USA) containing the cell growth supplements L-glutamine, amphotericin B, penicillin, streptomycin, and fetal bovine serum, without stimulatory supplements or vitamins. Cells were cultured in a humidified incubator at 37°C with 5% CO_2. hADMSCs passaged three times were used in all experiments.

For hADMSC spheroid formation, when hADMSCs reached 80% confluence at passage 2, the monolayer cells were enzymatically dissociated with 0.25% trypsin and EDTA. The cell suspension was counted using a LUNA-II (Logos Biosystems, Republic of Korea) cell counter and diluted to 1.2×10^5 cells ml^{-1}. Subsequently, cells were transferred to StemFIT 3D plate (MiocroFIT, Republic of Korea) and incubated for 2 days at 37°C with 5% CO_2.

To cultivate the hADMSCs in the PLGA microscaffold and microrobot, we sterilized the PLGA microscaffolds and microrobots with 70% ethanol for 30 min and washed them twice with PBS. The 10 PLGA microscaffolds and microrobots were then transferred to wells of an ultralow attachment round-bottom 96-well plate (Corning, USA), and hADMSCs were seeded onto them. The hADMSC-PLGA microscaffold and hADMSC-microrobot were cultured in a humidified incubator at 37°C with 5% CO_2, and the complete medium was replaced every 3 days.

Statistics and data analysis

Comparisons of all experimental data were analyzed using Student's *t* test. All data were presented as the mean ± SD. The differences between groups of $^*P < 0.05$ were considered as statistically significant, and $^{**}P < 0.01$ and $^{***}P < 0.001$ were considered as highly significant.

SUPPLEMENTARY MATERIALS

robotics.sciencemag.org/cgi/content/full/5/38/eaay6626/DC1
Materials and Methods
Section S1. Materials of the microrobot
Section S2. Fabrication of the microrobot
Section S3. Actuation principles of the microrobot
Section S4. Control principle and optimal coil placement of the EMA system
Section S5. Characterization and calibration of the EMA system
Section S6. Experimental setup for microrobot targeting tests using the EMA system
Section S7. Experimental setup for fixation and adhesion tests of the microrobot
Section S8. Cell viability assay
Section S9. Evaluation of cell proliferation and loading of the microrobot
Section S10. Chondrogenic differentiation
Section S11. Reverse transcription polymerase chain reaction and real-time polymerase chain reaction
Section S12. Animals
Section S13. Evaluation of inflammatory responses to PLGA microscaffold and microrobot
Section S14. Histological and immunohistochemical analysis
Fig. S1. SEM images of PLGA microscaffolds after w-o-w emulsion–based gelatin leaching.
Fig. S2. PLGA microscaffold does not affect chondrogenic differentiation.
Fig. S3. Cartilage-specific gene expression gradually increases with the period of chondrogenic differentiation.
Fig. S4. Phantom with patella and medial condyle defect models for microrobot targeting test using a single magnet.
Fig. S5. Microrobot targeting with and without magnet at patella and medial condyle defect models.
Fig. S6. Experimental setup of EMA system and arthroscope for ex vivo targeting test on the porcine knee joint.
Fig. S7. Microrobot mobility in aqueous solution with different viscosity.
Fig. S8. Numerical simulation result of fluid flow by different directions of microrobot injection.
Fig. S9. Time-lapse image sequence of microrobots without magnetic targeting at the defect of medial condyle (left) and patella (right) in ex vivo porcine knee.
Fig. S10. A single magnet helps magnetic fixation of microrobot located at patella cartilage defects.
Fig. S11. Illustration and numerical simulation of microrobot fixation for medial condyle defects using the magnet placed on tibia.
Fig. S12. Numerical simulation results of magnetic field gradient generated from a magnet in defect region.
Fig. S13. Fluorescence image of engrafted hADMSC in cartilage tissue.
Fig. S14. Histological analysis of cartilage regeneration by microrobot system.
Fig. S15. Upper and lower regions of coil placement.
Fig. S16. First and last coil configurations among coil configuration candidates obtained through the optimization routine.
Fig. S17. Characterization and calibration of EMA system.
Fig. S18. Experimental setup for magnetic fixation of microrobot.
Table S1. Design parameters of the EMA system.
Table S2. Specifications of the EMA system with optimal coil configuration.
Table S3. Angle range of coils within the region of coil placement (fig. S15).
Table S4. Comparison between first and last coil configurations (fig. S16) for the coil configuration candidate obtained through the optimization routine.
Movie S1. Microrobot targeting with and without magnet at patella and medial condyle defect models.
Movie S2. Manipulation of microrobots in a knee joint phantom.
Movie S3. 3D magnetic targeting of microrobots in five phantoms with a hole.
Movie S4. Magnetic targeting of microrobots in ex vivo porcine knee cartilage at medial condyle and patella defects.
Movie S5. Magnetic fixation of microrobots in ex vivo porcine knee cartilage.
Movie S6. Adhesion of hADMSC-microrobots in ex vivo porcine knee cartilage.
Movie S7. Magnetic targeting of hADMSC-microrobots in rabbit knee cartilage with a medial condyle defect.
References (*48*–*52*)

REFERENCES AND NOTES

1. C. Madeira, A. Santhagunam, J. B. Salgueiro, J. M. S. Cabral, Advanced cell therapies for articular cartilage regeneration. *Trends Biotechnol.* **33**, 35–42 (2015).
2. A. Mobasheri, G. Kalamegam, G. Musumeci, M. E. Batt, Chondrocyte and mesenchymal stem cell-based therapies for cartilage repair in osteoarthritis and related orthopaedic conditions. *Maturitas* **78**, 188–198 (2014).
3. T. Negoro, Y. Takagaki, H. Okura, A. Matsuyama, Trends in clinical trials for articular cartilage repair by cell therapy. *npj Regen. Med.* **3**, 17 (2018).
4. G. Filardo, F. Perdisa, A. Roffi, M. Marcacci, E. Kon, Stem cells in articular cartilage regeneration. *J. Orthop. Surg. Res.* **11**, 42 (2016).
5. U. Nöth, A. F. Steinert, R. S. Tuan, Technology insight: Adult mesenchymal stem cells for osteoarthritis therapy. *Nat. Clin. Pract. Rheumatol.* **4**, 371–380 (2008).
6. E. A. Makris, A. H. Gomoll, K. N. Malizos, J. C. Hu, K. A. Athanasiou, Repair and tissue engineering techniques for articular cartilage. *Nat. Rev. Rheumatol.* **11**, 21–34 (2014).
7. B. D. Smith, D. A. Grande, The current state of scaffolds for musculoskeletal regenerative applications. *Nat. Rev. Rheumatol.* **11**, 213–222 (2015).

Downloaded from https://www.science.org at The Hong Kong University of Science and Technology (Guangzhou) on May 26, 2026

8. A. Goldberg, K. Mitchell, J. Soans, L. Kim, R. Zaidi, The use of mesenchymal stem cells for cartilage repair and regeneration: A systematic review. *J. Orthop. Surg. Res.* **12**, 39 (2017).
9. T. D. Bornes, A. B. Adesida, N. M. Jomha, Mesenchymal stem cells in the treatment of traumatic articular cartilage defects: A comprehensive review. *Arthritis Res. Ther.* **16**, 432 (2014).
10. J. Li, X. Li, T. Luo, R. Wang, C. Liu, S. Chen, D. Li, J. Yue, S.-h. Cheng, D. Sun, Development of a magnetic microrobot for carrying and delivering targeted cells. *Sci. Robot.* **3**, eaat8829 (2018).
11. S. Jeon, S. Kim, S. Ha, S. Lee, E. Kim, S. Y. Kim, S. H. Park, J. H. Jeon, S. W. Kim, C. Moon, B. J. Nelson, J.-y. Kim, S.-W. Yu, H. Choi, Magnetically actuated microrobots as a platform for stem cell transplantation. *Sci. Robot.* **4**, eaav4317 (2019).
12. I. C. Yasa, A. F. Tabak, O. Yasa, H. Ceylan, M. Sitti, 3D-printed microrobotic transporters with recapitulated stem cell niche for programmable and active cell delivery. *Adv. Funct. Mater.* **29**, 1808992 (2019).
13. X.-Z. Chen, J.-H. Liu, M. Dong, L. Müller, G. Chatzipirpiridis, C. Hu, A. Terzopoulou, H. Torlakcik, X. Wang, F. Mushtaq, J. Puigmartí-Luis, Q.-D. Shen, B. J. Nelson, S. Pané, Magnetically driven piezoelectric soft microswimmers for neuron-like cell delivery and neuronal differentiation. *Mater. Horiz.* **6**, 1512–1516 (2019).
14. G. Go, J. Han, J. Zhen, S. Zheng, A. Yoo, M.-J. Jeon, J.-O. Park, S. Park, A magnetically actuated microscaffold containing mesenchymal stem cells for articular cartilage repair. *Adv. Healthc. Mater.* **6**, 1601378 (2017).
15. S.-W. Choi, Y. Zhang, Y.-C. Yeh, A. Lake Wooten, Y. Xia, Biodegradable porous beads and their potential applications in regenerative medicine. *J. Mater. Chem.* **22**, 11442–11451 (2012).
16. X. Wang, X.-H. Qin, C. Hu, A. Terzopoulou, X.-Z. Chen, T.-Y. Huang, K. Maniura-Weber, S. Pané, B. J. Nelson, 3D printed enzymatically biodegradable soft helical microswimmers. *Adv. Funct. Mater.* **28**, 1804107 (2018).
17. M. Barrow, A. Taylor, P. Murray, M. J. Rosseinsky, D. J. Adams, Design considerations for the synthesis of polymer coated iron oxide nanoparticles for stem cell labelling and tracking using MRI. *Chem. Soc. Rev.* **44**, 6733–6748 (2015).
18. B. Chen, Y. Li, X. Zhang, F. Liu, Y. Liu, Minji, F. Xiong, N. Gu, An efficient synthesis of ferumoxytol induced by alternating-current magnetic field. *Mater. Lett.* **170**, 93–96 (2016).
19. J. P. Bullivant, S. Zhao, B. J. Willenberg, B. Kozissnik, C. D. Batich, J. Dobson, Materials characterization of feraheme/ferumoxytol and preliminary evaluation of its potential for magnetic fluid hyperthermia. *Int. J. Mol. Sci.* **14**, 17501–17510 (2013).
20. G. Unsoy, S. Yalcin, R. Khodadust, G. Gunduz, U. Gunduz, Synthesis optimization and characterization of chitosan-coated iron oxide nanoparticles produced for biomedical applications. *J. Nanopart. Res.* **14**, 964 (2012).
21. C. Guo, R. A. Gemeinhart, Understanding the adsorption mechanism of chitosan onto poly(lactide-co-glycolide) particles. *Eur. J. Pharm. Biopharm.* **70**, 597–604 (2008).
22. S. Akmaz, E. Dilaver Adıgüzel, M. Yasar, O. Erguven, The effect of Ag content of the chitosan-silver nanoparticle composite material on the structure and antibacterial activity. *Adv. Mater. Sci. Eng.* **2013**, 690918 (2013).
23. Y. Wang, P. Li, L. Kong, Chitosan-modified PLGA nanoparticles with versatile surface for improved drug delivery. *AAPS PharmSciTech* **14**, 585–592 (2013).
24. S. Yu, G. M. Chow, Carboxyl group (–CO_2H) functionalized ferrimagnetic iron oxide nanoparticles for potential bio-applications. *J. Mater. Chem.* **14**, 2781–2786 (2004).
25. E. A. Elhefian, M. M. Nasef, A. H. Yahaya, Preparation and characterization of chitosan/agar blended films: Part 2. thermal, mechanical, and surface properties. *J. Chem.* **9**, 510–516 (2012).
26. F. N. Almajhdi, H. Fouad, K. A. Khalil, H. M. Awad, S. H. S. Mohamed, T. Elsarnagawy, A. M. Albarrag, F. F. Al-Jassir, H. S. Abdo, In-vitro anticancer and antimicrobial activities of PLGA/silver nanofiber composites prepared by electrospinning. *J. Mater. Sci. Mater. Med.* **25**, 1045–1053 (2014).
27. E. Vey, C. Rodger, J. Booth, M. Claybourn, A. F. Miller, A. Saiani, Degradation kinetics of poly(lactic-co-glycolic) acid block copolymer cast films in phosphate buffer solution as revealed by infrared and Raman spectroscopies. *Polym. Degrad. Stab.* **96**, 1882–1889 (2011).
28. A. R. Costa-Pinto, A. M. Martins, M. J. Castelhano-Carlos, V. M. Correlo, P. C. Sol, A. Longatto-Filho, M. Battacharya, R. L. Reis, N. M. Neves, In vitro degradation and in vivo biocompatibility of chitosan–poly(butylene succinate) fiber mesh scaffolds. *J. Bioact. Compat. Polym.* **29**, 137–151 (2014).
29. R. M. Bennett, J. L. Skosey, Lactoferrin and lysozyme levels in synovial fluid. *Arthritis Rheum.* **20**, 84–90 (1977).
30. L. Lu, S. J. Peter, M. D. Lyman, H.-L. Lai, S. M. Leite, J. A. Tamada, S. Uyama, J. P. Vacanti, L. Robert, A. G. Mikos, In vitro and in vivo degradation of porous poly(dl-lactic-*co*-glycolic acid) foams. *Biomaterials* **21**, 1837–1845 (2000).
31. E. E. Mahmoud, G. Kamei, Y. Harada, R. Shimizu, N. Kamei, N. Adachi, N. A. Misk, M. Ochi, Cell magnetic targeting system for repair of severe chronic osteochondral defect in a rabbit model. *Cell Transplant.* **25**, 1073–1083 (2016).
32. J. Niu, Q. Qi, Y. Niu, C. Dong, Z. Dong, P. Cui, F. Wang, Patella morphological alteration after patella instability in growing rabbits. *J. Orthop. Surg. Res.* **12**, 106 (2017).
33. P. Duan, Z. Pan, L. Cao, Y. He, H. Wang, Z. Qu, J. Dong, J. Ding, The effects of pore size in bilayered poly (lactide-co-glycolide) scaffolds on restoring osteochondral defects in rabbits. *J. Biomed. Mater. Res. A* **102**, 180–192 (2014).
34. E. H. Jebens, M. E. Monk-Jones, On the viscosity and pH of synovial fluid and the pH of blood. *J. Bone Joint Surg.* **41**, 388–400 (1959).
35. D. Choudhury, R. Walker, T. Roy, S. Paul, R. Mootanah, Performance of honed surface profiles to artificial hip joints: An experimental investigation. *Int. J. Precis. Eng. Manuf.* **14**, 1847–1853 (2013).
36. J. Hori, M. Deie, T. Kobayashi, Y. Yasunaga, S. Kawamata, M. Ochi, Articular cartilage repair using an intra-articular magnet and synovium-derived cells. *J. Orthop. Res.* **29**, 531–538 (2011).
37. S. Panseri, A. Russo, M. Sartori, G. Giavaresi, M. Sandri, M. Fini, M. C. Maltarello, T. Shelyakova, A. Ortolani, A. Visani, V. Dediu, A. Tampieri, M. Marcacci, Modifying bone scaffold architecture in vivo with permanent magnets to facilitate fixation of magnetic scaffolds. *Bone* **56**, 432–439 (2013).
38. C. D. Hoemann, J. Sun, A. Légaré, M. D. McKee, M. D. Buschmann, Tissue engineering of cartilage using an injectable and adhesive chitosan-based cell-delivery vehicle. *Osteoarthr. Cartil.* **13**, 318–329 (2005).
39. S. J. Nho, M. J. Pensak, D. A. Seigerman, B. J. Cole, Rehabilitation after autologous chondrocyte implantation in athletes. *Clin. Sports Med.* **29**, 267–282 (2010).
40. T. J. Brown, U. B. Laurent, J. R. Fraser, Turnover of hyaluronan in synovial joints: Elimination of labelled hyaluronan from the knee joint of the rabbit. *Exp. Physiol.* **76**, 125–134 (1991).
41. L. A. Mundt, K. Shanahan, *Graff's Textbook of Routine Urinalysis and Body Fluids* (Lippincott Williams & Wilkins, 2010).
42. T. M. Tamer, Hyaluronan and synovial joint: Function, distribution and healing. *Interdiscip. Toxicol.* **6**, 111–125 (2013).
43. E. Cukierman, R. Pankov, K. M. Yamada, Cell interactions with three-dimensional matrices. *Curr. Opin. Cell Biol.* **14**, 633–640 (2002).
44. F. Rosso, A. Giordano, M. Barbarisi, A. Barbarisi, From cell–ECM interactions to tissue engineering. *J. Cell. Physiol.* **199**, 174–180 (2004).
45. U. Akgun, B. Kocaoglu, S. Ergun, M. Karahan, M. Turkmen, The effect of environmental pH change on bovine articular cartilage metabolism: Implications for the use of buffered solution during arthroscopy? *Knee Surg. Sports Traumatol. Arthrosc.* **22**, 2843–2848 (2014).
46. A. B. Pai, A. O. Garba, Ferumoxytol: A silver lining in the treatment of anemia of chronic kidney disease or another dark cloud? *J. Blood Med.* **3**, 77–85 (2012).
47. D. Hetzel, W. Strauss, K. Bernard, Z. Li, A. Urboniene, L. F. Allen, A Phase III, randomized, open-label trial of ferumoxytol compared with iron sucrose for the treatment of iron deficiency anemia in patients with a history of unsatisfactory oral iron therapy. *Am. J. Hematol.* **89**, 646–650 (2014).
48. A. J. Petruska, B. J. Nelson, Minimum bounds on the number of electromagnets required for remote magnetic manipulation. *IEEE Trans. Robot.* **31**, 714–722 (2015).
49. D. Son, M. D. Dogan, M. Sitti, Magnetically actuated soft capsule endoscope for fine-needle aspiration biopsy, paper presented at the 2017 IEEE International Conference on Robotics and Automation (ICRA), Singapore, Singapore, 29 May to 3 June 2017.
50. A. Pourkand, J. J. Abbott, A critical analysis of eight-electromagnet manipulation systems: The role of electromagnet configuration on strength, isotropy, and access. *IEEE Robot. Automat. Lett.* **3**, 2957–2962 (2018).
51. M. P. Kummer, J. J. Abbott, B. E. Kratochvil, R. Borer, A. Sengul, B. J. Nelson, OctoMag: An electromagnetic system for 5-DOF wireless micromanipulation. *IEEE Trans. Robot.* **26**, 1006–1017 (2010).
52. J. L. Cook, C. T. Hung, K. Kuroki, A. M. Stoker, C. R. Cook, F. M. Pfeiffer, S. L. Sherman, J. P. Stannard, Animal models of cartilage repair. *Bone Joint Res.* **3**, 89–94 (2014).

Acknowledgments: We thank the Medical Microrobot Center at the Chonnam National University for providing facilities. **Funding:** This research was supported by the Bio & Medical Technology Development Program of the National Research Foundation (NRF) funded by the Korean government (MSIT) (2016M3A9E9941514). Moreover, this research was supported by a grant from the Korea Health Technology R&D Project through the Korea Health Industry Development Institute (KHIDI), funded by the Ministry of Health and Welfare, Republic of Korea (grant number HI19C0642). **Author contributions:** Experimental design was conceived and developed by G.G., S.-G.J., and E.C. with assistance from C.-S.K., E.K.S., Y.J., J.K.S., and J.-O.P. Scaffolds were designed and fabricated by G.G., S.K., and Z.J. EMA system was designed and fabricated by G.G., K.T.N., B.K., and C.-S.K. Fixation device was designed and fabricated by G.G. Cell-related experiments were performed by G.G., S.-G.J., A.Y., Y.R.S., J.Y.K., and J.Y.N. In vivo experiments were performed by G.G., S.-G.J., A.Y., J.H., Y.R.S., J.Y.K., J.Y.N., and J.K.S. The

Downloaded from https://www.science.org at The Hong Kong University of Science and Technology (Guangzhou) on May 26, 2026

manuscript was written by G.G., S.-G.J., S.K., and E.C. with edits and inputs provided by all other authors. **Competing interests:** G.G., B.K., J.H., and J.-O.P. are inventors on U.S. patent application 16/097,714; G.G., B.K., J.H., C.-S.K., E.C., and J.-O.P. are inventors on U.S. patent application 16/015,662; and G.G. and J.-O.P. are inventors on U.S. patent application 10/004,566. All patent applications were submitted by the Chonnam National University and cover the stem cell–based microrobot. The other authors declare that they have no competing interests. **Data and materials availability:** All the data needed to evaluate the study are in the main text or in the Supplementary Materials. Contact E.C. for additional data or materials.

Submitted 11 July 2019
Accepted 17 December 2019
Published 22 January 2020
10.1126/scirobotics.aay6626

Citation: G. Go, S.-G. Jeong, A. Yoo, J. Han, B. Kang, S. Kim, K. T. Nguyen, Z. Jin, C.-S. Kim, Y. R. Seo, J. Y. Kang, J. Y. Na, E. K. Song, Y. Jeong, J. K. Seon, J.-O. Park, E. Choi, Human adipose–derived mesenchymal stem cell–based medical microrobot system for knee cartilage regeneration in vivo. *Sci. Robot.* **5**, eaay6626 (2020).

Downloaded from https://www.science.org at The Hong Kong University of Science and Technology (Guangzhou) on May 26, 2026

Science Robotics

Human adipose–derived mesenchymal stem cell–based medical microrobot system for knee cartilage regeneration in vivo

Gwangjun Go, Sin-Gu Jeong, Ami Yoo, Jiwon Han, Byungjeon Kang, Seokjae Kim, Kim Tien Nguyen, Zhen Jin, Chang-Sei Kim, Yu Ri Seo, Ju Yeon Kang, Ju Yong Na, Eun Kyoo Song, Yongyeon Jeong, Jong Keun Seon, Jong-Oh Park, and Eunpyo Choi

Sci. Robot. **5** (38), eaay6626. DOI: 10.1126/scirobotics.aay6626

View the article online
https://www.science.org/doi/10.1126/scirobotics.aay6626
Permissions
https://www.science.org/help/reprints-and-permissions

Downloaded from https://www.science.org at The Hong Kong University of Science and Technology (Guangzhou) on May 26, 2026

Use of this article is subject to the Terms of service

Science Robotics (ISSN 2470-9476) is published by the American Association for the Advancement of Science. 1200 New York Avenue NW, Washington, DC 20005. The title *Science Robotics* is a registered trademark of AAAS.

Copyright © 2020 The Authors, some rights reserved; exclusive licensee American Association for the Advancement of Science. No claim to original U.S. Government Works